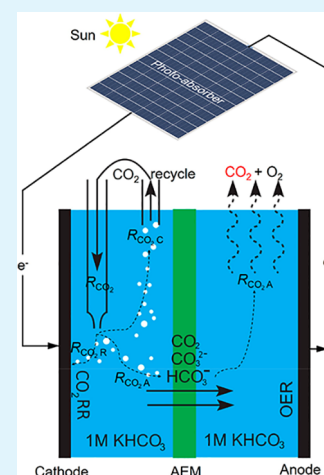# An Experimental- and Simulation-Based Evaluation of the CO_2 Utilization Efficiency of Aqueous-Based Electrochemical CO_2 Reduction Reactors with Ion-Selective Membranes

Meng Lin,[†,‡] Lihao Han,[†,‡] Meenesh R. Singh,*[§] and Chengxiang Xiang*[†,‡]

†Joint Center for Artificial Photosynthesis, and Division of Chemistry and Chemical Engineering, and ‡Division of Chemistry and Chemical Engineering, California Institute of Technology, Pasadena, California 91125, United States
§Department of Chemical Engineering, University of Illinois at Chicago, Chicago, Illinois 60607, United States

Ⓢ Supporting Information

ABSTRACT: The CO_2 utilization efficiency of three types of electrochemical CO_2 reduction (CO_2R) reactors by using different ion-selective membranes, including anion exchange membrane (AEM), cation exchange membrane (CEM), and bipolar membrane (BPM), was studied quantitatively via both experimental and simulation methods. The operating current density of the CO_2R reactors was chosen to be between 10 and 50 mA cm^{-2} to be relevant for solar-fuel devices with relatively low photon flux from sunlight. In the AEM-based CO_2R reactor with a six-electron per carbon CO_2R at the cathode surface, an upper limit of 14.4% for the CO_2 utilization efficiency was revealed by modeling and validated by experimental measurements in CO_2-saturated aqueous electrolytes without any buffer electrolyte. Improvements in CO_2 utilization efficiency were observed when additional buffer electrolyte was added into the aqueous solution, especially in solutions with low bicarbonate concentrations. The effects of the feed rate of the input CO_2 stream, the Faradaic efficiency (FE), and the participating electron numbers of the cathode reaction on the CO_2 utilization efficiency were also studied in the AEM-based CO_2R reactor. The CEM-based CO_2R reactor exhibited low CO_2 utilization efficiency with recirculation between the catholyte and the anolyte and was unsustainable due to the cation depletion from the anolyte without any recirculation. The BPM-based CO_2R reactor operated continuously without a significant increase in the cell voltage and exhibited significantly higher CO_2 utilization efficiency, up to 61.4%, as compared to the AEM-based CO_2R reactors. Diffusive CO_2 loss across the BPM resulted in relatively low CO_2 utilization efficiency at low operating current densities. Modeling and simulation also provided target BPM properties for higher CO_2 utilization efficiency and efficient cell operation.

KEYWORDS: electrochemical CO_2 reduction, CO_2 utilization efficiency, ion exchange membrane, modeling, ionic conductivity, bipolar membrane

INTRODUCTION

Electrochemical and photoelectrochemical (PEC) CO_2 reduction (CO_2R) into value-added fuels or chemicals have become an active area of research in the past few years.[1−9] Significant advances have been made in the materials discovery and device architecture for selective and efficient CO_2R reactions.[3,10−15] In aqueous-based CO_2R systems, ion selective membranes, such as cation exchange membrane (CEM), anion exchange membrane (AEM), or bipolar membrane (BPM), have been widely used to minimize the product crossovers and to provide ionic conductions between the cathode and anode chambers. In particular, the bipolar membrane-based reactors have been of significant interest[16−20] due to its ability to maintain pH differentials between the cathode and the anode chambers. Solar-driven CO_2 reduction devices that used bipolar membrane exhibited solar-to-fuel (STF) conversion efficiencies that exceeded 10% for CO generation[21] and for formate generation.[22] AEM-based solar-driven CO_2 reduction devices

have also shown promising conversion efficiency to oxygenate and hydrocarbons.[23,24] On the modeling side, although there have been several studies[25−27] on the effects of local pHs and local CO_2 concentrations on the operating conditions and constraints for CO_2R reactors, the CO_2 utilization efficiency is often overlooked or sacrificed in fundamental studies and in the materials discovery research to maintain a well-controlled reaction environment with constant CO_2 concentrations.[28] However, the utilization efficiency will have a significant impact on the overall efficiency of the system and the cost of the produced fuels or chemicals in practical devices. This study focuses on the analysis of the CO_2 utilization behavior of membrane-based reactors. More specifically, the rate of CO_2 crossover to the anode chamber and the CO_2 utilization
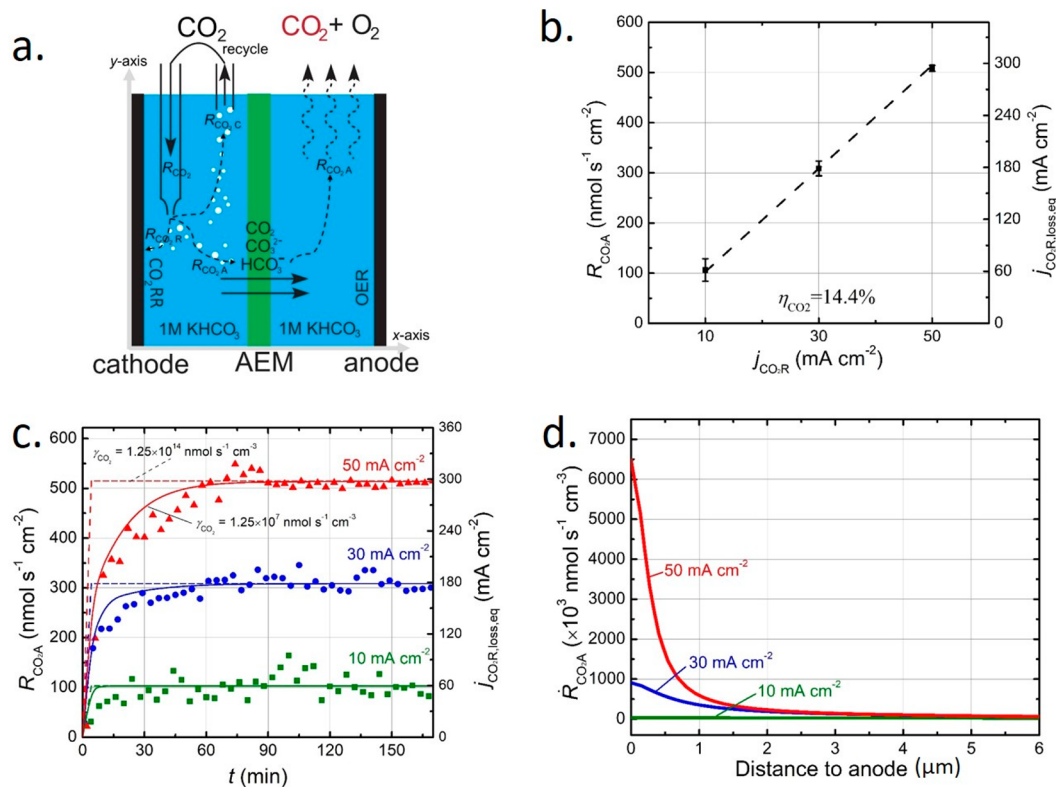
Figure 1. (a) Schematic illustration of the AEM-based CO_2R reactor. (b) CO_2 loss rate (R_{CO_2A}) and the equivalent CO_2 current density loss ($j_{CO_2R,loss,eq}$) as a function of operating current density. (c) Transient behavior of R_{CO_2A} and $j_{CO_2R,loss,eq}$ of AEM cell for different operating current densities (50 mA cm^{-2} in red, 30 mA cm^{-2} in blue, and 10 mA cm^{-2} in green) with two CO_2 releasing coefficients (γ_{CO_2}). (d) Volumetric CO_2 loss rate ($\dot{R}_{CO_2A}$) distribution as a function of distance from anode to cathode surfaces for applied current densities of 10, 30, and 50 mA cm^{-2}. Dots with error bars are experimental data, and solid and dashed line are simulation data. The 1D simulation is performed along the x-axis.

efficiency were modeled, simulated, and experimentally measured in aqueous-based electrochemical devices with CEMs, AEMs, and BPMs and a range of electrolyte conditions. The simulation and the experimental results revealed significant challenges in improving the CO_2 utilization efficiency in aqueous-based configurations, especially with higher electron CO_2R products.

RESULTS AND DISCUSSION

Figure 1a shows the pathways of CO_2 transport in a generic aqueous-based electrochemical CO_2R device, in which the cathode for CO_2R reaction and the anode for oxygen evolution reaction (OER) are separated by an AEM separator that facilitates the ionic transport between the catholyte and anolyte. The CO_2 utilization efficiency (η_{CO_2}), which is defined as the CO_2 utilized per unit amount of CO_2 fed to the utilization process,[24] can be written as follows:

$$\eta_{CO_2} = \frac{R_{CO_2R}}{R_{CO_2R} + R_{CO_2A} + R_{CO_2C}} \times 100\% \quad (1)$$

where R_{CO_2C} is the rate of the unreacted CO_2 leaving the cathode chamber, $R_{CO_2R} = \frac{\eta_F j_{total}}{nF}$ is the rate of CO_2R reaction at the cathode surface (n is the number of electrons participating in CO_2R reaction, F is the Faraday constant, j_{total} is the total geometric current density of the cathode, and η_F is the Faradaic efficiency for CO_2R reaction), and R_{CO_2A} is the

rate of the CO_2 loss across the separator to the anode chamber in the form of CO_2, HCO_3^-, and CO_3^{2-}. $R_{CO_2} = R_{CO_2R} + R_{CO_2A} + R_{CO_2C}$ is the total rate of CO_2 feed to the cathode chamber. All the rates in eq 1 are normalized with respect to the unit area of the cathode. While the rate of the unreacted CO_2 leaving the cathode chamber can be optimized and minimized in principle with multipass reactor designs, the CO_2 transported across the separator (R_{CO_2A}) would eventually coevolve with O_2 from the anode and would result in significant energy penalties to bring an O_2-free, relatively pure stream of CO_2 back to the cathode. The R_{CO_2A} was measured experimentally and evaluated computationally in this study.

In the AEM-based CO_2R reactor (Figure 1a), the CO_2 transport across the separator, the electrolyte concentrations, and the resulting upper limit for the CO_2 utilization efficiency are independent of the overpotential of cathodic reaction. The generation rate of OH^- at the cathode electrode, which controls the electrolyte composition in the cathode chamber, is independent of the cathodic reaction and is only determined by the operating current density of the electrode. As a result, as long as the catholyte is saturated with CO_2, the rate of HCO_3^- crossing through the AEM is independent of the cathodic reactions. The effect of cathodic reactions on R_{CO_2A} is shown in Figure S1, showing no difference in R_{CO_2A} between CO_2R reaction with unity Faradaic efficiency and the hydrogen evolution (HER) case. Therefore, a Ni cathode was used for
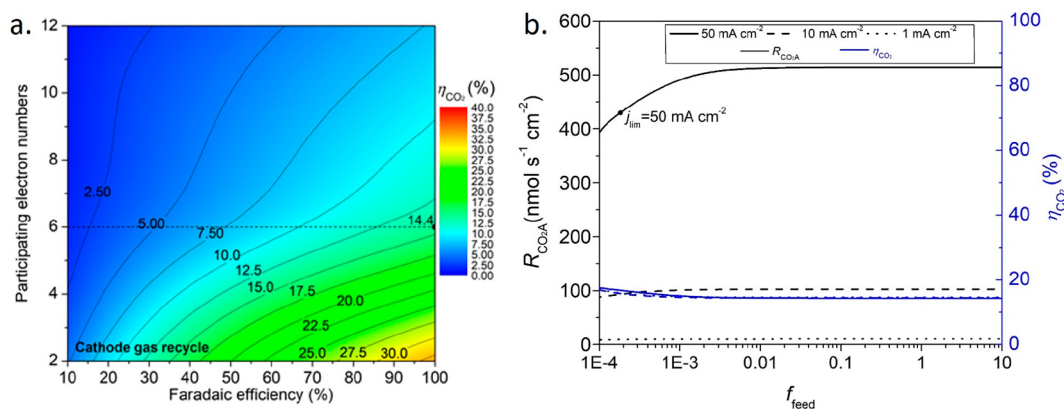
Figure 2. (a) CO_2 utilization efficiency (η_{CO_2}) as a function of CO_2R participating electron numbers and Faradaic efficiency without considering R_{CO_2C} (cathode gas recycle). (b) R_{CO_2A} and η_{CO_2} as a function of reduced cathode CO_2 feed rate by a factor of f_{feed} at operating current density of 1, 10, and 50 mA cm^{-2}.

HER, instead of CO_2R, to mimic the pH gradient and OH^- generation rate in the system as well as to simplify the experimental measurements and validations. This is implemented for all the experiments performed in this study. Furthermore, the electrochemical rates for the hydroxide generation and proton generation at the surface of the cathode and anode were held constant during the modeling and experimental measurements. While the concentration increase of CO_2R products during the reaction would change the equilibrium potential of the reaction, the electrode potential would be adjusted accordingly to maintain the constant operating current density. The anolyte was prebubbled with CO_2 gas without any circulation or stirring to ensure an initial equilibrium of the anolyte, AEM, and catholyte. The plasticization of membranes was not observed during the course of the measurements. Furthermore, the stable cell potential in AEM-based (Figure S2c) and BPM-based (Figure S8c) reactors confirms the ionic properties of membranes were not changing significantly throughout the experiment. The lower range of operating current density, 10−50 mA cm^{-2}, chosen in this study to evaluate CO_2 utilization efficiency of the device, is comparable to the operating photocurrent density of a solar-driven CO_2R system (without solar concentration).[21−24,29−31] This will offer direct design guidelines for solar-driven CO_2R reactors using various unconcentrated photoabsorbers.

In the AEM-based CO_2R reactor, the HCO_3^- was the dominating ionic current carrier crossing the separator, which can be confirmed from Figure S2b showing that the HCO_3^- crossover current density, $j_{HCO_3^-}$, was 9.9 mA cm^{-2} at the operating current density of 10 mA cm^{-2}. The crossed-over HCO_3^- eventually contributed to the CO_2 loss close to anode surface due to the acidic environment at anode boundary layer region favoring dehydration of HCO_3^- to CO_2. From the nucleation theory,[25,32] the CO_2 loss at the anode chamber was modeled as a volumetric source term that was dependent on the CO_2 supersaturation (S) and a CO_2 loss coefficient (γ_{CO_2}) (see eq S11). In addition, the CO_2 loss was experimentally measured in the gas mixture evolving from the anode chamber by using gas chromatography (see experimental method section in the Supporting Information). Figure 1b shows R_{CO_2A} as a function of operating current density at the cathode surface for CO_2R. The anodic CO_2 loss due to crossover (R_{CO_2A}) can also be represented as an equivalent loss in the CO_2R current density, which is defined as follows and shown in Figure 1b:

$$j_{CO_2R,loss,eq} = nFR_{CO_2A} \qquad (2)$$

The simulation results show that R_{CO_2A} and $j_{CO_2R,loss,eq}$ increase linearly with increasing operating current density at the cathode (dashed line in Figure 1b). At the steady state, the simulation results suggest that all the HCO_3^- ions that were crossing over the AEM contributed to the release of CO_2 gas from the anode chamber. For instance, the rate of CO_2 loss of R_{CO_2A} = 103 nmol s^{-1} cm^{-2} was a consequence of the HCO_3^- current density of $j_{HCO_3^-}$ = 9.9 mA cm^{-2} crossing the AEM at the operating current density of 10 mA cm^{-2}. The experimentally measured R_{CO_2A} (dots with error bars in Figure 1b) at various operating current density were in close agreement with the simulation results, confirming the mechanism of CO_2 loss in electrochemical or photoelectrochemical devices. Assuming the rate of the unreacted CO_2 leaving the cathode chamber, R_{CO_2C} = 0 with ideal multipass reactor design, an upper limit of CO_2 utilization efficiency (η_{CO_2}) of 14.4% was found for all applied current densities for a six-electron CO_2R reaction at the cathode (e.g., C_2H_4 or C_2H_5OH) independent of the operating current density of the device. The result suggests that in an aqueous-based CO_2R reactor with AEM the CO_2 loss to the anode chamber is ∼6 times higher than the CO_2 used and converted at the cathode. Note that the η_{CO_2} varies as the number of electrons per mole of CO_2 involved in CO_2R reaction changes. From eqs 1 and 2, the calculated values of η_{CO_2} were 33.3%, 20%, and 11.1%, for 2-, 4-, and 8-electron CO_2R products, respectively (see Figure 2a).

Figure 1c shows the transient behavior of the rate of CO_2 gas release from the anode chamber. The green, blue, and red data points show the experimental CO_2 gas release rate as a function of time when the reactor operated at 10, 30, and 50 mA cm^{-2}, respectively. After the initial increase, the R_{CO_2A} and the corresponding $j_{CO_2R,loss,eq}$ reached a steady-state value for all three current densities. Transport analysis of the cell was then performed to understand the transient behavior as well as the
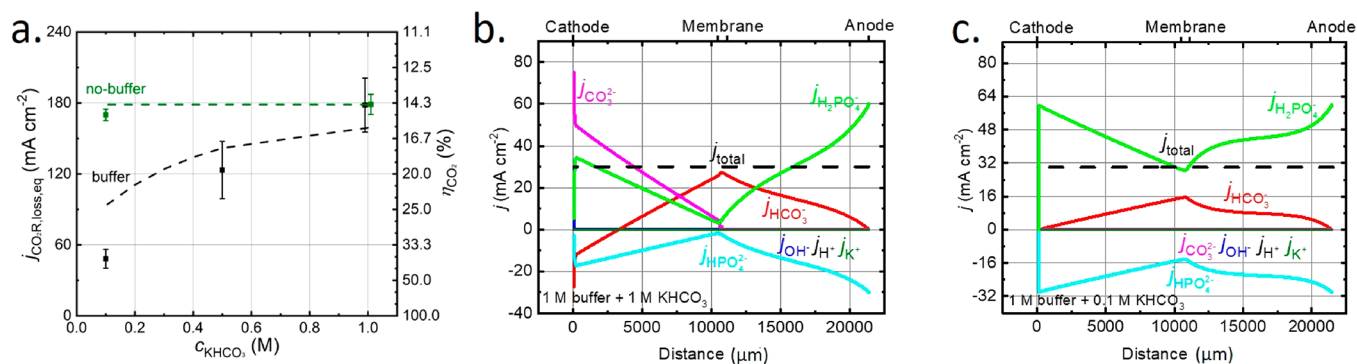
Figure 3. (a) $j_{CO_2R,loss,eq}$ and η_{CO_2} as a function of $KHCO_3$ concentration with 1 M phosphate buffer solution at an operating current density of 30 mA cm^{-2}. The no-buffer case (0.1 and 1 M $KHCO_3$) was plotted in green as a reference. Dots with error bars are experimental data, and lines are simulation data. (b) Partial current density as a function of distance from the cathode surface for the case with 1 M $KHCO_3$ and 1 M phosphate buffer solution under an applied current density of 30 mA cm^{-2} at steady-state conditions. (c) Partial current density as a function of distance from the cathode surface for the case with 0.1 M $KHCO_3$ and 1 M phosphate buffer solution under an applied current density of 30 mA cm^{-2} at steady-state conditions.

spatial distribution of the $CO_2(g)$ release rates. Two values of the CO_2 releasing coefficient (γ_{CO_2}) were used and compared in this study, i.e., $\gamma_{CO_2} = 1.25 \times 10^{14}$ and 1.25×10^7 nmol s^{-1} cm^{-3}. While both values resulted in the same steady-state values of R_{CO_2A}, the former value (1.25×10^{14} nmol s^{-1} cm^{-3}), which was reported by Wilt,[32] resulted in a large discrepancy at the initial stage of the operation (0–60 min) shown as dashed lines in Figure 1c. By reduction of the value of γ_{CO_2} to 1.25×10^7 nmol s^{-1} cm^{-3}, the transient behavior of the CO_2 gas release rate (Figure 1c, solid lines) matched relatively well with the experimental results. The CO_2 releasing coefficient (γ_{CO_2}) represented the gaseous CO_2 escaping rate (nmol s^{-1}) per unit volume (m^{-3}) electrolyte. γ_{CO_2} is closely related to the nucleation rate of CO_2, which is highly dependent on the properties (roughness, wettability, etc.) of the electrodes, the properties of electrolyte, and the operating current densities. The releasing coefficient also depends exponentially on the contact angle and the roughness of the surface where gas bubbles are nucleating. Wilt[32] showed that the rate of nucleation could vary over 7 orders of magnitude with changes in the surface roughness. In this study, the lower value of CO_2 releasing coefficient is likely due to the smoother electrode surface with fewer sites to nucleate CO_2 bubbles. The simulations for all other reactors were performed with this corrected γ_{CO_2} value.

Figure 1d shows the simulated spatial distribution of R_{CO_2A} as a function of distance from the anode surface. The R_{CO_2A} was significantly higher close to the anode surface and decreased drastically with the increasing distance from the anode surface, indicating a strong influence of pH on the nucleation of CO_2 gas in the aqueous electrolyte. The simulation results also suggested that the majority of the nucleation for CO_2 evolution occurred within ~1 μm distance from the anode surface, which agreed well with a previous study by Wilt and others.[32]

Figure 2a shows the effects of Faradaic efficiency (FE) and participation electron numbers for CO_2R reaction on the η_{CO_2}. Higher FE and lower participation electron numbers exhibited higher η_{CO_2}. For example, at an FE of 100% for a two-electron CO_2RR, the η_{CO_2} can reach up to 33.3% as compared to 14.4%

for the reference case with a 100% FE and six-electron CO_2RR. Note that the results are independent of operation current density according to eq 1 as long as R_{CO_2C} is equal to 0 (ideal case for cathode gas recycling). In a more realistic case ($R_{CO_2C} > 0$) when the cathode gas recycling is not considered, the η_{CO_2} was much smaller (Figure S3a). For example, a constant CO_2 flow of 5 sccm is considered for a 1 cm^2 area electrode undergoing six-electron CO_2R reaction with 100% FE; the maximum η_{CO_2} was 2.3% at an operating current density of 50 mA cm^{-2} (Figure S3a).

One approach to increase the η_{CO_2} is to reduce the CO_2 feed rate while keeping the same operating current density for the cell. Figure 2b shows the R_{CO_2A} and the corresponding η_{CO_2} as a function of reduced cathode CO_2 feed rate at three different operating current densities. The CO_2 feed rate (R_{feed}) was defined as follows: $R_{feed} = f_{feed} \times k_{feed} \times c_{CO_2}$, where the k_{feed} is 0.33 s^{-1} based on literature data[25] corresponding to ~21 sccm for the 10 mL cathode chamber in this study and c_{CO_2} is the electrolyte CO_2 concentration. The η_{CO_2} remained nearly constant (Figure 2b) even when the CO_2 feed rate was reduced by 10^4 times for all three operating current densities. Further reduction of the CO_2 feed rate resulted in a significant increase of the bulk pH of the catholyte and a significant decrease of the dissolved CO_2 near the cathode electrode and lowering the limiting current density of the cell (Figure S3b). For instance, when the f_{feed} was reduced to $<1.8 \times 10^{-4}$, the limiting current density of the cell was limited to <50 mA cm^{-2}. In the extreme case where f_{feed} was reduced to 1.5×10^{-5}, the bulk pH of the electrolyte reached 10.1 in the steady-state operation, and OH$^-$ contributed to the ionic transport through the AEM, a η_{CO_2} of 71.2% was obtained at the limiting current density of the cell at 2.8 mA cm^{-2}. In addition, we also showed that the CO_2 loss rate is independent of the spacing between the electrode and membrane (see Figure S4).

The R_{CO_2A} in the AEM-based CO_2 reactor was mainly due to the dominating partial current density of HCO$_3^-$ across the separator. One strategy to minimize the transference of HCO$_3^-$ across the AEM is to introduce supporting anions (current carriers) in the solution, such as adding a high concentration of buffers. Figure 3 shows the experimental and
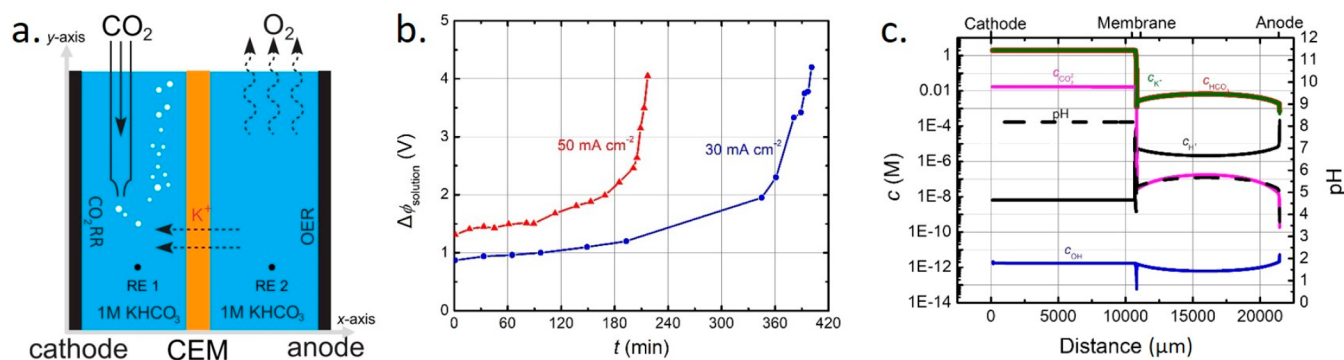
Figure 4. (a) Schematic illustration of the CEM-based CO_2R reactor. Two reference electrodes (RE 1 and RE 2, black dots) were placed at the middle of cathode and anode for the quantification of the voltage drop across separator and electrolyte. (b) Experimentally measured voltage loss due to mass transport in the electrolyte and CEM (voltage difference between two reference electrodes) as a function of time for the applied current densities of 30 mA cm^{-2} (in blue) and 50 mA cm^{-2} (in red). (c) Species concentration and pH as a function of distance from the cathode surface for the case for the applied current density of 30 mA cm^{-2} at $\Delta\phi_{solution}$ = 4 V.

modeling results of the R_{CO_2A} and the corresponding η_{CO_2} when 1 M phosphate buffer solution was added into various $KHCO_3$ (0.1, 0.5, and 1 M) solutions. The phosphate buffer species ($H_2PO_4^-$ and HPO_4^{2-}) were equilibrated according to its pK_a of 6.9 in the CO_2-saturated solutions of pH = 7.85 for 1 M $KHCO_3$, pH = 7.55 for 0.5 M $KHCO_3$, and pH = 6.58 for 0.1 M $KHCO_3$. The detailed buffer compositions are listed in Table S5. The near-neutral pH conditions used in this study were the dominating pH environments in reported CO_2R studies due to the lack of dissolved CO_2 in alkaline conditions (very low operating current density) and the poor selectivity for CO_2R in acidic conditions (very high selectivity toward HER).[25] In general, the reactors with buffered electrolytes exhibited a higher CO_2 utilization efficiency for various concentrations of $KHCO_3$ solutions. The dashed green line and the dashed black line represent the simulated values of $j_{CO_2R,loss,eq}$ and the η_{CO_2} as a function of the HCO_3^- concentration for the unbuffered and buffered (1 M phosphate buffer) solutions, respectively. The simulated η_{CO_2} increased from 14.4% to 15.9% in 1 M $KHCO_3$ solution when 1 M phosphate buffer electrolyte was added. The simulated η_{CO_2} was further increased up to ~24% by reducing the concentration of $KHCO_3$ to 0.1 M in a 1 M phosphate buffer solution. The experimentally measured $j_{CO_2R,loss,eq}$ and the corresponding η_{CO_2} (dots with error bars in Figure 3a, also see transient data in Figure S5a) showed a similar trend as compared to the simulation results. The measured η_{CO_2} was 14.4%, 19.6%, and 38.3% for 1, 0.5, and 0.1 M $KHCO_3$ case, respectively. The discrepancy between simulation and the experimental results with low bicarbonate concentrations could be due to the concentration-dependent diffusion coefficient of HCO_3^- in AEM and in the buffered solutions (see the Supporting Information and Figure S6). To further understand the effect of buffer on the CO_2 crossover, spatial distributions of the partial ionic current of various species were obtained at the steady-state operation of the electrochemical CO_2R reactor. Figure 3b shows the steady-state spatial distribution of ionic current densities for all anions and cations in 1 M $KHCO_3$ solution with 1 M phosphate buffer at the operational current density of 30 mA cm^{-2}. The partial current density of cations H$^+$ and K$^+$ was close to zero, whereas the anions have either positive or negative current density, indicating the

primary mechanism of transport being either migration or diffusion, respectively. The net current density of CO_2 carriers such as HCO_3^- and CO_3^{2-} was positive and in the direction away from the cathode.

The addition of a buffer reduces marginally the transference of HCO_3^-, while the majority of the current density across the AEM was still supported by HCO_3^- (red curve). The calculated partial current densities of HCO_3^-, CO_3^{2-}, $H_2PO_4^-$, and HPO_4^{2-} were 26.5, 3.5, 2, and −2 mA cm^{-2}, respectively. As a result of a marginal reduction in the transference of HCO_3^-, negligible improvement in η_{CO_2} was observed when buffer electrolytes were added into the 1 M $KHCO_3$ solution. Substantial improvement in η_{CO_2} was observed by lowering the concentration of the $KHCO_3$ solution by an order of magnitude, which, in turn, reduced the partial current density and transference of HCO_3^- across the AEM (see Figure 3c). As seen in Figure 3c, the partial current carried by $H_2PO_4^-$ and HPO_4^{2-} increased to 28.3 and 13.9 mA cm^{-2} when reducing the $KHCO_3$ to 0.1 M while keeping the buffer solution concentration at 1 M. This leads to reduced partial current densities of HCO_3^- and CO_3^{2-} (15.8 and ~0 mA cm^{-2}) resulting in an enhanced η_{CO_2}.

Another strategy to reduce the transference of HCO_3^- and hence the CO_2 loss is to use a CEM in the electrochemical CO_2R device. Figure 4 shows the schematic illustration of an aqueous, CEM-based CO_2R reactor. Figure 4a shows that although the CEM-based CO_2R reactors have the potential to minimize CO_2 crossover by blocking the HCO_3^- transport, the cell cannot be operated at steady state without recirculation due to the excessive potential losses associated with electrodialysis. Figure 4b shows the experimentally measured values of the voltage drop due to the solution transport losses ($\Delta\phi_{solution}$) at two different current densities. The $\Delta\phi_{solution}$ increased as a function of time for both operating current densities until the cell potential exceeded the limit of the potentiostat (up to 11 V, see Figure S7b). In the near-neutral pH conditions, the K$^+$ was the dominating current carried across the CEM (see Figure S7a). While proton generation rate at the anode was the same as the K$^+$ crossover rate through the CEM, the proton generated at the anode surface combined with carbonate ions to generate CO_2 that get escaped from the anolyte and mixed with the produced O_2 to the anode outlet. This leads to a decreased conductivity of anolyte, resulting in
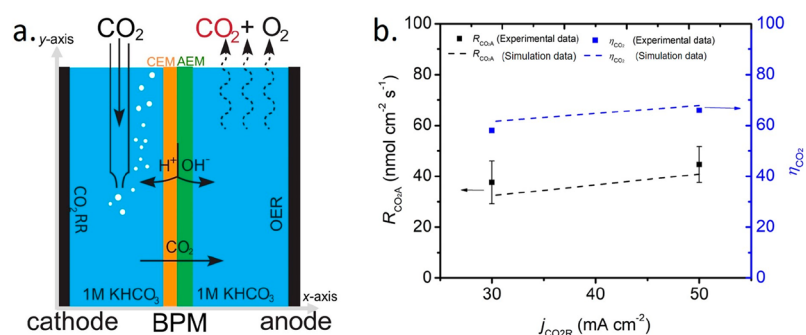
Figure 5. (a) Schematic illustration of the BPM-based CO_2R reactor with 1 M $KHCO_3$. (b) R_{CO_2A} and the corresponding η_{CO_2} as a function of the operating current density for both experimental data (dots) and simulation data (dashed lines).
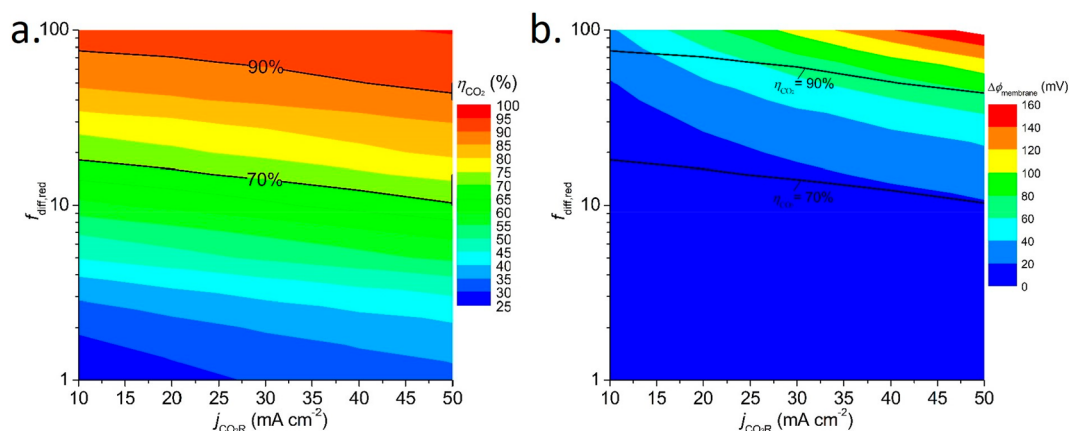

Figure 6. (a) Contour map of η_{CO_2} as a function of $CO_2(aq)$ diffusion coefficient reduction factor ($f_{diff,red}$) and j_{CO_2R} for the BPM-based CO_2R reactor. (b) Contour map of $\Delta\phi_{membrane}$ as a function of $f_{diff,red}$ and j_{CO_2R} for the BPM-based CO_2R reactor.

continuous increase in cell voltage (see Figure 4c) and the increased pH gradients.[33] Figure 4c shows the spatial distribution of all ionic species' concentrations (solid lines) and pH (black dashed line) values across the CEM-based CO_2R reactor at an operating current density of 30 mA cm^{-2} at 400 min after the cell operation. The average concentration of K$^+$ (c_{K^+}) dropped below 0.01 M in anolyte, resulting in the large electrolyte conductivity decrease and unsustainable operation of the reactor. The nonlinear behavior of $\Delta\phi_{solution}$ as a function of the operation time was also a result of the reciprocal relation between transport loss and electrolyte conductivity (see eq S15). In principle, the depletion of the cation in the anolyte can be circumvented by convective recirculation between the catholyte and anolyte.[34] However, the recirculation and mixing between the catholyte and the anolyte would lead to a significant increase in R_{CO_2A} due to the effective transport of the dissolved CO_2 to the anode chamber (see Figure S7c). The recirculation of electrolyte increased the value of R_{CO_2A} to 97 nmol s^{-1} cm^{-2} and decreased the corresponding η_{CO_2} to 15.1% at an operating current density of 10 mA cm^{-2} (Figure S7c), which was comparable to the CO_2 loss in the AEM-based CO_2 reactor without recirculation.

To circumvent the electrodialysis loss in a CEM-based CO_2 reactor without recirculation, a BPM can be used to facilitate the ion transport between the cathode and the anode and to block the HCO_3^- anion crossover to the anode. Figure 5a shows the schematic illustration of the BPM-based CO_2R reactor. BPM is composed of a CEM component (colored

orange) and an AEM (colored green) component. Instead of allowing specific ions to pass through the BPM, water was disassociated into H$^+$ and OH$^-$ at the BPM interface and transported to catholyte and anolyte through CEM and AEM layers, respectively. Figure 5b shows the modeling (dashed lines) and the experimental measurements (dots) of the steady-state behavior of R_{CO_2A} and the corresponding η_{CO_2} at two different operating current densities −30 and 50 mA cm^{-2}. The simulated R_{CO_2A} values at steady-state conditions reached 32.4 and 40.9 nmol cm^{-2} s^{-1} for 30 and 50 mA cm^{-2}, respectively. Correspondingly, the experimentally measured R_{CO_2A} were 37.6 and 44.6 nmol cm^{-2} s^{-1} for 30 and 50 mA cm^{-2} (averaged value for the test range of 400−500 min), respectively, showing a reasonable agreement between simulation and experimental results. The transient behavior of R_{CO_2A} and the corresponding $j_{CO_2R,loss,eq}$ can be found in Figure S8d. The CO_2 loss at steady state was driven primarily by the diffusion of the dissolved CO_2 across the BPM. A slightly higher R_{CO_2A}, which corresponds to a larger CO_2 concentration differential between the catholyte and anolyte, at higher operating current densities was observed because the higher release rate of CO_2 at the anode surface lowered the average CO_2 concentration in anolyte. For example, the average CO_2 concentrations in the anolyte were 20.1 and 15 mM for 30 and 50 mA cm^{-2}, respectively. The η_{CO_2} in the BPM-based CO_2R reactor were 58.0% and 61.4% for 30 and 50 mA cm^{-2} for the six-electron CO_2R reaction, which was

significantly higher than that of AEM-based reactor (14.4%). Despite the improved η_{CO_2} in the BPM-based reactor compared to the AEM-based CO_2R reactor, the η_{CO_2} was still limited to 61.4% at the operating current density of 50 mA cm^{-2} (see Figure 5b) for a six-electron per mole of product CO_2R reaction. Further improvement in η_{CO_2} for the BPM-based reactor requires a reduction in the diffusion coefficient of dissolved CO_2 in BPM. Figure 6 shows contour maps of the η_{CO_2} and the additional potential drop across BPM ($\Delta\phi_{membrane}$) as a function of the operating current density when a series of reduction factors of the CO_2 diffusion coefficient in BPM were used. The simulation results show that reductions in the diffusion coefficient by 77 and 44 times were required to achieve η_{CO_2} of 90% for 10 and 50 mA cm^{-2}, respectively (see the solid line in Figure 6a). Correspondingly, the additional potential drop across BPM ($\Delta\phi_{membrane}$) was relatively low (<80 mV) to achieve a η_{CO_2} of 90% for a range of operating current densities from 10 to 50 mA cm^{-2} (see Figure 6b). For a target η_{CO_2} of 70%, reductions in the diffusion coefficient in BPM by 18 and 10 times were required for 10 and 50 mA cm^{-2}. This offers a practical design guideline for the design of BPM to achieve higher η_{CO_2}.

CONCLUSIONS

In summary, the CO_2 utilization efficiency in membrane-based electrochemical CO_2R reactors was quantitatively evaluated by modeling and experimental methods. The transport of the HCO_3^- across the AEM in AEM-based CO_2R reactors significantly limited the CO_2 utilization efficiency of the device. In AEM-based CO_2R reactors, an operating-current-density-independent CO_2 utilization efficiency with an upper limit of 14.4% were observed by modeling and experiments in the CO_2-saturated aqueous electrolytes without any buffer electrolyte for six-electron per mole of product CO_2R reaction with unity FE and ideal gas recycling. Lower FEs and nonideal gas recycling further decreased the CO_2 utilization efficiency in AEM-based CO_2R reactor. To operate at a current density of 10−50 mA cm^{-2} for solar-fuel devices, the reduction of the CO_2 feed in the cathode chamber did not improve the CO_2 utilization efficiency and started to limit the operating current density due to the increase of the bulk electrolyte pH. In the AEM-based reactor, the CO_2 utilization efficiency was improved from 14.4% to 38.3% when a 1 M phosphate buffer solution was added in the 0.1 M bicarbonate solution. The CEM-based CO_2R reactor exhibited low CO_2 utilization efficiency with recirculation between the catholyte and the anolyte and was unsustainable due to the cation depletion from the anolyte without any recirculation. The BPM-based CO_2R reactor operated continuously without any significant increase in the cell voltage and exhibited significantly higher CO_2 utilization efficiency, up to 61.4%, as compared to the AEM-based CO_2R reactors. Further improvement in CO_2 utilization efficiency in the BPM-based reactor requires a reduction in the diffusion coefficient of CO_2 in the membrane. For example, a η_{CO_2} of 90% can be achieved by reducing the CO_2 diffusion coefficient by ~77 times at 50 mA cm^{-2} without any significant increase in the voltage drop across the BPM. The study revealed significant challenges in CO_2 utilization efficiency in aqueous-based electrochemical cells operating at current densities that are relevant to solar-fuel devices and also provided design guidelines for membrane-based electrochemical or photoelectrochemical CO_2R reactors to achieve higher CO_2 utilization efficiencies.

ASSOCIATED CONTENT

Ⓢ Supporting Information

The Supporting Information is available free of charge on the ACS Publications website at DOI: 10.1021/acsaem.9b00986.

Additional simulation results for AEM-, CEM-, and BPM-based reactors; transient CO_2 loss behavior for buffered AEM-based reactor; transient behavior of reactor voltage for CEM-based reactor; simulation method; and experimental method (PDF)

AUTHOR INFORMATION

Corresponding Authors
*E-mail cxx@caltech.edu.
*E-mail mrsingh@uic.edu.

ORCID Ⓞ
Meng Lin: 0000-0001-7785-749X
Lihao Han: 0000-0002-0452-3381
Meenesh R. Singh: 0000-0002-3638-8866
Chengxiang Xiang: 0000-0002-1698-6754

Author Contributions
M.L. and L.H. contributed equally to this work.

Notes
The authors declare no competing financial interest.

REFERENCES

(1) Li, K.; Peng, B.; Peng, T. Recent Advances in Heterogeneous Photocatalytic CO_2 Conversion to Solar Fuels. *ACS Catal.* **2016**, *6* (11), 7485−7527.

(2) Zhou, X.; Liu, R.; Sun, K.; Chen, Y.; Verlage, E.; Francis, S. A.; Lewis, N. S.; Xiang, C. Solar-Driven Reduction of 1 Atm of CO_2 to Formate at 10% Energy-Conversion Efficiency by Use of a TiO_2-Protected III−V Tandem Photoanode in Conjunction with a Bipolar Membrane and a Pd/C Cathode. *ACS Energy Lett.* **2016**, *1* (4), 764−770.

(3) Jouny, M.; Luc, W.; Jiao, F. High-Rate Electroreduction of Carbon Monoxide to Multi-Carbon Products. *Nat. Catal.* **2018**, *1* (10), 748.

(4) Dinh, C.-T.; Burdyny, T.; Kibria, M. G.; Seifitokaldani, A.; Gabardo, C. M.; Garcia de Arquer, F. P.; Kiani, A.; Edwards, J. P.; De Luna, P.; Bushuyev, O. S.; Zou, C.; Quintero-Bermudez, R.; Pang, Y.; Sinton, D.; Sargent, E. H. CO_2 Electroreduction to Ethylene via Hydroxide-Mediated Copper Catalysis at an Abrupt Interface. *Science (Washington, DC, U. S.)* **2018**, *360* (6390), 783−787.

(5) Jhong, H. R. M.; Ma, S.; Kenis, P. J. Electrochemical Conversion of CO_2 to Useful Chemicals: Current Status, Remaining Challenges,

and Future Opportunities. *Curr. Opin. Chem. Eng.* **2013**, *2* (2), 191−199.

(6) Zhuang, T.-T.; Pang, Y.; Liang, Z.-Q.; Wang, Z.; Li, Y.; Tan, C.-S.; Li, J.; Dinh, C. T.; De Luna, P.; Hsieh, P.-L.; Burdyny, T.; Li, H.-H.; Liu, M.; Wang, Y.; Li, F.; Proppe, A.; Johnston, A.; Nam, D.-H.; Wu, Z.-Y.; Zheng, Y.-R.; Ip, A. H.; Tan, H.; Chen, L.-J.; Yu, S.-H.; Kelley, S. O.; Sinton, D.; Sargent, E. H. Copper Nanocavities Confine Intermediates for Efficient Electrosynthesis of C3 Alcohol Fuels from Carbon Monoxide. *Nat. Catal.* **2018**, *1* (12), 946−951.

(7) Zhou, Y.; Che, F.; Liu, M.; Zou, C.; Liang, Z.; De Luna, P.; Yuan, H.; Li, J.; Wang, Z.; Xie, H.; Li, H.; Chen, P.; Bladt, E.; Quintero-Bermudez, R.; Sham, T. K.; Bals, S.; Hofkens, J.; Sinton, D.; Chen, G.; Sargent, E. H. Dopant-Induced Electron Localization Drives CO₂reduction to C2hydrocarbons. *Nat. Chem.* **2018**, *10* (9), 974−980.

(8) Cook, R. L. High Rate Gas Phase CO₂ Reduction to Ethylene and Methane Using Gas Diffusion Electrodes. *J. Electrochem. Soc.* **1990**, *137* (2), 607.

(9) Lu, Q.; Jiao, F. Electrochemical CO₂ Reduction: Electrocatalyst, Reaction Mechanism, and Process Engineering. *Nano Energy* **2016**, *29*, 439−456.

(10) Yang, H. B.; Hung, S.-F.; Liu, S.; Yuan, K.; Miao, S.; Zhang, L.; Huang, X.; Wang, H.-Y.; Cai, W.; Chen, R.; Gao, J.; Yang, X.; Chen, W.; Huang, Y.; Chen, H. M.; Li, C. M.; Zhang, T.; Liu, B. Atomically Dispersed Ni(i) as the Active Site for Electrochemical CO₂ Reduction. *Nat. Energy* **2018**, *3* (2), 140−147.

(11) Jiang, K.; Siahrostami, S.; Zheng, T.; Hu, Y.; Hwang, S.; Stavitski, E.; Peng, Y.; Dynes, J.; Gangisetty, M.; Su, D.; Attenkofer, K.; Wang, H. Isolated Ni Single Atoms in Graphene Nanosheets for High-Performance CO₂reduction. *Energy Environ. Sci.* **2018**, *11* (4), 893−903.

(12) Weekes, D. M.; Salvatore, D. A.; Reyes, A.; Huang, A.; Berlinguette, C. P. Electrolytic CO₂ Reduction in a Flow Cell. *Acc. Chem. Res.* **2018**, *51* (4), 910−918.

(13) Zhu, S.; Jiang, B.; Cai, W.-B.; Shao, M. Direct Observation on Reaction Intermediates and the Role of Bicarbonate Anions in CO₂ Electrochemical Reduction Reaction on Cu Surfaces. *J. Am. Chem. Soc.* **2017**, *139* (44), 15664−15667.

(14) Verma, S.; Lu, X.; Ma, S.; Masel, R. I.; Kenis, P. J. A. The Effect of Electrolyte Composition on the Electroreduction of CO₂ to CO on Ag Based Gas Diffusion Electrodes. *Phys. Chem. Chem. Phys.* **2016**, *18* (10), 7075−7084.

(15) Han, L.; Zhou, W.; Xiang, C. High-Rate Electrochemical Reduction of Carbon Monoxide to Ethylene Using Cu-Nanoparticle-Based Gas Diffusion Electrodes. *ACS Energy Lett.* **2018**, *3* (4), 855−860.

(16) Lv, J.; Jouny, M.; Luc, W.; Zhu, W.; Zhu, J.; Jiao, F. A Highly Porous Copper Electrocatalyst for Carbon Dioxide Reduction. *Adv. Mater.* **2018**, *30* (49), 1803111.

(17) Li, Y. C.; Zhou, D.; Yan, Z.; Gonçalves, R. H.; Salvatore, D. A.; Berlinguette, C. P.; Mallouk, T. E. Electrolysis of CO₂ to Syngas in Bipolar Membrane-Based Electrochemical Cells. *ACS Energy Lett.* **2016**, *1* (6), 1149−1153.

(18) Vermaas, D. A.; Smith, W. A. Synergistic Electrochemical CO₂ Reduction and Water Oxidation with a Bipolar Membrane. *ACS Energy Lett.* **2016**, *1* (6), 1143−1148.

(19) Vermaas, D. A.; Wiegman, S.; Nagaki, T.; Smith, W. A. Ion Transport Mechanisms in Bipolar Membranes for (Photo) Electrochemical Water Splitting. *Sustain. Energy Fuels* **2018**, *2* (9), 2006−2015.

(20) Salvatore, D. A.; Weekes, D. M.; He, J.; Dettelbach, K. E.; Li, Y. C.; Mallouk, T. E.; Berlinguette, C. P. Electrolysis of Gaseous CO₂ to CO in a Flow Cell with a Bipolar Membrane. *ACS Energy Lett.* **2018**, *3* (1), 149−154.

(21) Schreier, M.; Heroguel, F.; Steier, L.; Ahmad, S.; Luterbacher, J. S.; Mayer, M. T.; Luo, J.; Gratzel, M. Solar Conversion of CO₂ to CO Using Earth-Abundant Electrocatalysts Prepared by Atomic Layer Modification of CuO. *Nat. Energy* **2017**, *2* (7), 17087.

(22) Zhou, X.; Liu, R.; Sun, K.; Chen, Y.; Verlage, E.; Francis, S. A.; Lewis, N. S.; Xiang, C. Solar-Driven Reduction of 1 Atm of CO₂ to Formate at 10% Energy-Conversion Efficiency by Use of a TiO₂-Protected III-V Tandem Photoanode in Conjunction with a Bipolar Membrane and a Pd/C Cathode. *ACS Energy Lett.* **2016**, *1* (4), 764−770.

(23) Gurudayal; Bullock, J.; Srankó, D. F.; Towle, C. M.; Lum, Y.; Hettick, M.; Scott, M. C.; Javey, A.; Ager, J. Efficient Solar-Driven Electrochemical CO 2 Reduction to Hydrocarbons and Oxygenates. *Energy Environ. Sci.* **2017**, *10* (10), 2222−2230.

(24) Gurudayal; Beeman, J. W.; Bullock, J.; Wang, H.; Eichhorn, J.; Towle, C.; Javey, A.; Toma, F. M.; Mathews, N.; Ager, J. W. Si Photocathode with Ag-Supported Dendritic Cu Catalyst for CO₂ Reduction. *Energy Environ. Sci.* **2019**, *12* (3), 1068−1077.

(25) Singh, M. R.; Clark, E. L.; Bell, A. T. Effects of Electrolyte, Catalyst, and Membrane Composition and Operating Conditions on the Performance of Solar-Driven Electrochemical Reduction of Carbon Dioxide. *Phys. Chem. Chem. Phys.* **2015**, *17* (29), 18924−18936.

(26) Chen, Y.; Lewis, N. S.; Xiang, C. Modeling and Simulation of the Spatial and Light-Intensity Dependence of Product Distributions in an Integrated Photoelectrochemical CO₂ Reduction System. *ACS Energy Lett.* **2016**, *1* (1), 273−280.

(27) Hashiba, H.; Weng, L. C.; Chen, Y.; Sato, H. K.; Yotsuhashi, S.; Xiang, C.; Weber, A. Z. Effects of Electrolyte Buffer Capacity on Surface Reactant Species and the Reaction Rate of CO₂in Electrochemical CO₂reduction. *J. Phys. Chem. C* **2018**, *122* (7), 3719−3726.

(28) Li, Y. C.; Yan, Z.; Hitt, J.; Wycisk, R.; Pintauro, P. N.; Mallouk, T. E. Bipolar Membranes Inhibit Product Crossover in CO₂ Electrolysis Cells. *Adv. Sustain. Syst.* **2018**, *2* (4), 1700187.

(29) Arai, T.; Sato, S.; Morikawa, T. A Monolithic Device for CO₂ Photoreduction to Generate Liquid Organic Substances in a Single-Compartment Reactor. *Energy Environ. Sci.* **2015**, *8* (7), 1998−2002.

(30) Sugano, Y.; Ono, A.; Kitagawa, R.; Tamura, J.; Yamagiwa, M.; Kudo, Y.; Tsutsumi, E.; Mikoshiba, S. Crucial Role of Sustainable Liquid Junction Potential for Solar-to-Carbon Monoxide Conversion by a Photovoltaic Photoelectrochemical System. *RSC Adv.* **2015**, *5* (67), 54246−54252.

(31) Jeon, H. S.; Koh, J. H.; Park, S. J.; Jee, M. S.; Ko, D.-H.; Hwang, Y. J.; Min, B. K. A Monolithic and Standalone Solar-Fuel Device Having Comparable Efficiency to Photosynthesis in Nature. *J. Mater. Chem. A* **2015**, *3* (11), 5835−5842.

(32) Wilt, P. M. Nucleation Rates and Bubble Stability in Water-Carbon Dioxide Solutions. *J. Colloid Interface Sci.* **1986**, *112* (2), 530−538.

(33) Singh, M. R.; Papadantonakis, K.; Xiang, C.; Lewis, N. S. An Electrochemical Engineering Assessment of the Operational Conditions and Constraints for Solar-Driven Water-Splitting Systems at near-Neutral PH. *Energy Environ. Sci.* **2015**, *8* (9), 2760−2767.

(34) Singh, M. R.; Xiang, C.; Lewis, N. Evaluation of Flow Schemes for Near-Neutral Electrolytes in Solar-Fuels Generators. *Sustain. Energy Fuels* **2017**, *1*, 458−466.